A Review Paper on Solving MRI-Related Issues through Additive Manufacturing

Miteshkumar Darji[1], Moinbhai Malek[2], Naitikkumar Patel[3], Shweta Gaur[4]

Students, Department of Instrumentation & Control Engineering[1,2,3]

Assistant Professor, Department of Instrumentation & Control Engineering[4]

Dharmsinh Desai University, Nadiad, Gujarat, India

Abstract: *This study uses cutting-edge materials and additive manufacturing (3D printing) to improve MRI technology. High-performance gradient coils are produced automatically by a 3D printing system and software, allowing for high-resolution imaging (50 μm) in a matter of seconds. A new multi-layer Litz wire addresses overheating in high-frequency applications such as cardiac imaging by reducing resistive losses by 80%. By using thin conductive layers, additive manufacturing also increases the MRI coils' flexibility and cooling. A 3D-printed tungsten collimator reduces eddy currents for SPECT/MRI integration, improving compatibility. MRI artifacts are reduced by 10% with lightweight titanium implants, namely those with a honeycomb cranioplasty design. Furthermore, ultra-short echo time (UTE) MRI provides a safe substitute for medical 3D printing by producing radiation-free 3D medical models with small deviations (<1.5 mm). These developments highlight the revolutionary potential of additive manufacturing in medical imaging by improving MRI efficiency, accuracy, and patient safety.*

Keywords: MRI, Litz wire, Additive manufacturing, RF coils

I. INTRODUCTION

Particularly in cardiac MRI, where quick pulse sequences are necessary to avoid image blurring from heart motion, the high pulse frequencies employed in MRI gradient and RF coils necessitate specific design techniques. Skin effects at frequencies higher than 10 kHz present problems for conventional wires, resulting in energy loss and overheating. Although foil-based designs have been investigated as a potential remedy, their use is restricted to two-layer configurations due to their inability to accommodate complex coil shapes and connecting problems. A viable substitute that makes use of fine aerosol jets to create ultra-thin conductive layers is additive manufacturing. Furthermore, cooling is still a crucial component of MRIs. By directly incorporating bioinspired fractal coolant channels into the coil structure, additive manufacturing techniques can improve cooling efficiency. By placing these embedded cooling channels microns away from heat-generating wires, thermal resistance may be considerably decreased, enhancing the overall effectiveness and performance of MRIs.

Multimodal imaging techniques have grown in importance over the last ten years, especially the combination of anatomical imaging techniques like Computed Tomography (CT) and Magnetic Resonance Imaging (MRI) with functional imaging techniques like Positron Emission Tomography (PET) and Single Photon Emission Computed Tomography (SPECT). With the advent of PET/MR hybrid imaging, it is now possible to combine the molecular and quantitative imaging capabilities of PET with the high soft tissue contrast of MRI. Whole-body PET/MR systems have changed from standalone imaging units to fully integrated platforms for simultaneous imaging since 2010. Likewise, preclinical SPECT/MRI systems have been created to combine the superior soft tissue contrast and biochemical data from MRI with the higher solution molecular imaging from SPECT. Clinical applications were made possible by early advancements like the first sequential small-animal SPECT/MRI system (Goetz et al., 2008) and simultaneous SPECT/MRI feasibility studies (Hamamura et al.). The goal of initiatives like INSERT is to combine SPECT and MRI in preclinical and clinical contexts. There is currently no commercial simultaneous SPECT/MRI system available, although Mediso has introduced a sequential preclinical SPECT/MRI system. Notwithstanding its promise, integrating SPECT and MRI presents many technological difficulties, most notably the existence of eddy currents in the collimator

brought on by pulsed magnetic field gradients. The quality of MRI images is impacted by these eddy currents because they distort the linear gradient fields in the region of interest. According to studies, the induced magnetic field can produce discernible distortions and reach up to 4.7% of the applied gradient field. This review investigates the use of new manufacturing techniques, such as additive manufacturing, to optimize collimator design in order to minimize these impacts.

Post-operative imaging issues have increased as a result of the growing usage of structural metal implants in contemporary surgery. Because implant materials and surrounding tissues have different magnetic characteristics, MRI, a crucial diagnostic technique, is susceptible to artifacts. These artifacts decrease the diagnostic accuracy for problems like infections or hemorrhages by distorting imaging, especially in high-field MRI systems ($\geq$3T).Implants made of titanium are frequently utilized because of their mechanical qualities and biocompatibility; they produce less artifacts than other metals, although their weak paramagnetism still makes imaging difficult. To reduce artifacts, a number of strategies have been investigated, such as implant coatings, alternate imaging sequences, and post-processing techniques. According to recent research, these distortions can be considerably reduced by employing Additive Manufacturing (AM) techniques to integrate porous materials and reduce implant mass. In order to enhance post-operative imaging and early complication diagnosis, this study explores the possibility of using lightweight, porous Ti-6Al-4V structures in implants to lessen MRI susceptibility artifacts.

In oral and maxillofacial surgery, the combination of additive manufacturing (AM) and virtual three-dimensional (3D) surgical planning is progressing, with notable promise for procedures including dental implants, tumor resections, reconstructions, and the restoration of mandibular fractures. By making it possible to create tailored implants, drill guides, and saw guides with improved predicted, functional, and cosmetic outcomes, these procedures help patients with anatomical restrictions, inadequate bone structure, or low bone density. Getting high-resolution 3D medical images in DICOM format, transforming them into Standard Tessellation Language (STL) files with virtual planning software, and creating constructs with computer-aided design (CAD) software are the three main phases in medical AM. MRI has been investigated as an alternative to computed tomography (CT), which has historically been utilized for implant design. However, because of the low proton density and quick T2 relaxation time of cortical bone, traditional MRI sequences are best suited for soft-tissue imaging and have trouble visualizing bone. Ultrashort echo time (UTE) MRI sequences were created to get around these restrictions, enabling quicker data collection and better bone imaging. PET/MRI attenuation correction, radiation planning, and MR-guided surgery are just a few of the sophisticated clinical uses for UTE MRI. Nevertheless, no research has examined UTE MRI's ability to produce AMsuitable STL models. Comparing the geometric accuracy of STL models produced from UTE MRI with morphological changes and flaws added throughout the AM process is the goal of this study.

II. FRACTAL COOLING IMPLEMENTED IN MRI GRADIENTCOIL

METHODS

Two additive manufacturing techniques were utilized for the construction of prototype coils. A unique fabrication approach was developed using spray-coating to propel and dry nano-inks and insulators, allowing for the deposition of layers 10-100 microns thick within seconds, exhibiting effective conductivity within and across interconnected layers. A second technique evaluated thicker layer applications, presumed to expedite the fabrication of larger coils. This system used a Fab@Home 3-D printer, designed with a computercontrolled gantry and a toolhead that extrudes material from a syringe to create components. A syringe-based system is advantageous for high output operations, especially when paired with precursor materials that possess a low solvent ratio. Such precursors are typically more viscous than those that can be applied through spray coating. Each layer underwent rapid heat treatment (approximately 60 seconds) using radiant heat prior to the application of the subsequent layer. Thicknesses over 1 mm can be deposited in a single pass with this technique, achieving resolutions between 0.1 - 1 mm based on the material used.

RESULTS

A. Modified Spray-Coat Technology:

Litz wires with various patterns were created using the spray coating method, resulting in a structure composed of four distinct metal layers and three insulator layers deposited on polycarbonate.
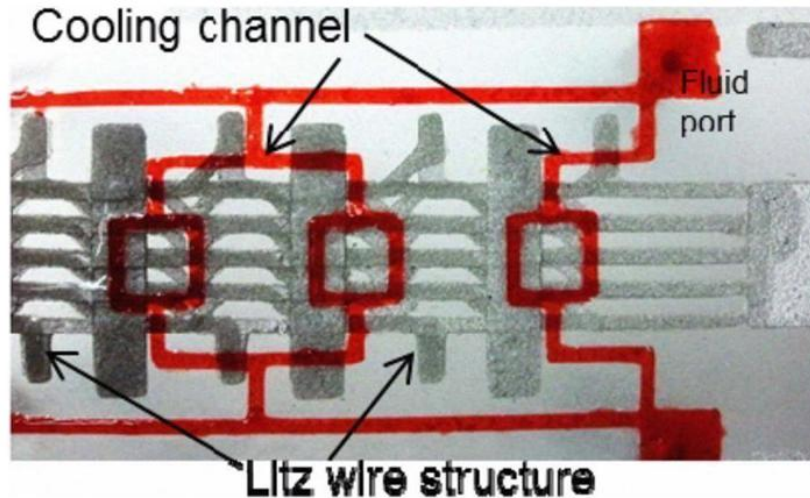

Image by "Goodbye Wires and Formers: 3-D Additive Manufacturing and Fractal Cooling Applied to Construction of MRI Gradient Coils"[1]

B. Syringe-Delivered Materials (Fab@Home)

Structures comprising up to seven layers (four metal layers, three insulator layers) were fabricated using this technique. A three-layer coil is illustrated in Fig.3, where two metal layers are separated by an insulating layer.

Typically, the resistances of coils with this configuration were below 200 mΩ, while the resistance between the top and bottom metal layers (when disconnected at the via) exceeded 30 MΩ. The typical resistivity for the metal layer measured under 10 μΩ-cm. Given the speed of operation for either method, it is feasible to build MRI gradient coils (about 10 cm tall) suitable for animal systems in less than a day.

III . MINIMIZING EDDY CURRENTS GENERATED BY MRI GRADIENT COILS

METHODS

A. Simulation Platform:

Gradient coils and collimators were simulated using FEKO, a three dimensional electromagnetic simulation software. FEKO employs the method of moments to deliver full-wave solutions to Maxwell's integral equations in the frequency space. The platform's time analysis feature also enabled electromagnetic problems to be evaluated in the time domain. Relevant computations were conducted in the frequency space, and fast Fourier transform algorithms were applied to convert data into the time domain. Frequency components of the gradient pulse were extracted via fast Fourier transform; a broadband simulation was then executed across the gradient shape frequency range. The simulation encompassed frequencies from 0 to 10 kHz to encompass a sinusoidal pulse with a 0.25 ms ramp-down time. Simulations were performed on x-, y-, and z-gradient coils for preclinical applications. The coils received currents of 167.24 A and 162.33 A for transverse and longitudinal gradient coils, respectively. The gradient strength was mT/m, with the maximum gradient deviation determined to be 2.06% and 0.86% for transverse and longitudinal gradient coils, correspondingly.
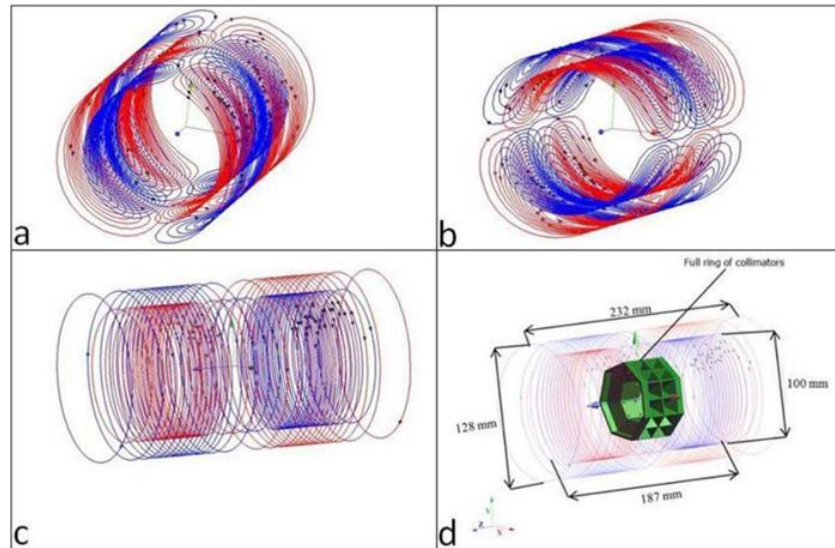
Image by "Simulated Design Strategies for SPECT Collimators to Reduce the Eddy Currents Induced by MRI Gradient Fields"[2]

B. Original Collimator

The newly designed collimator developed for a microSPECT system consists of seven identical collimators and digital silicon photomultipliers arranged in a ring. This setup remains stationary, minimizing sensitivity to geometric calibration challenges, making it more suitable for dynamic imaging and easier to integrate with MRI. Tungsten proves to be a viable material for MR-compatible collimators, offering high electron count and high density (19.25 g/cm³). However, pure tungsten is challenging to work with. It can be processed with tungsten alloys (comprising nickel, iron, and/or copper), which facilitate processing but result in reduced MR compatibility due to added susceptibility. Additive manufacturing addresses these challenges using selective laser melting techniques on pure tungsten powder. This method also permits variations in material density. The collimator supplier can provide densities ranging from 80% to 99%, which is significant as tungsten with lower density exhibits reduced conductivity, leading to minimal eddy currents. Yet, lower density also results in decreased attenuation coefficients. A density of 90% was chosen, and according to the Beer-Lambert Law, 2 mm of this material suffices to effectively attenuate 99.85% of incoming gamma rays at 140 keV.

C. System Optimization:

To lessen eddy currents in the collimator ring, modifications were made incrementally, examining the impact of each alteration. The magnetic field generated by eddy currents was calculated by comparing the z-component of the magnetic induction of the gradient coils without collimator to the z- component with the collimators. The focus on the z-component is due to its significance as the primary component for the gradient field. Various designs were simulated to diminish the magnetic field induced by eddy currents:

Smaller Flanges: Excess material was removed from the flanges on the edges of the collimator, which existed solely for mounting purposes and did not function to attenuate photons. This initial design adjustment involved minimizing the excess material in the flanges, where higher current densities would likely occur, while still ensuring proper mounting of the collimator.

Horizontal Slits: It was anticipated that current density would peak near the collimator's surface due to the skin effect, which could be reduced through surface slits. Spacing between the slits was maintained at 2 mm to avoid interference with collimator functionality.

Material Reduction in the Core: The collimator maintains a solid central tungsten core. Since photons are attenuated prior to reaching the core, this unnecessary material could be eliminated. Although this could further reduce eddy currents, it may complicate printing and necessitate a support structure.

Vertical Slit in the Middle: To diminish eddy currents without entirely eliminating core material, two vertical slits in the center of the collimator can be utilized (Fig. 3(D))

Z-shaped Vertical Slit: To optimally reduce eddy currents, the previous solutions (sections C.3 and C.4) can be merged (Fig. 3(E)). However, combining core material reduction with vertical slits may allow some photons to pass through the slits and the thin wall of the loft hole. This issue can be addressed by employing a Z-shaped slit (Fig. 3(F) and Fig. 4) instead of the vertical slit depicted in Fig. 3(D).
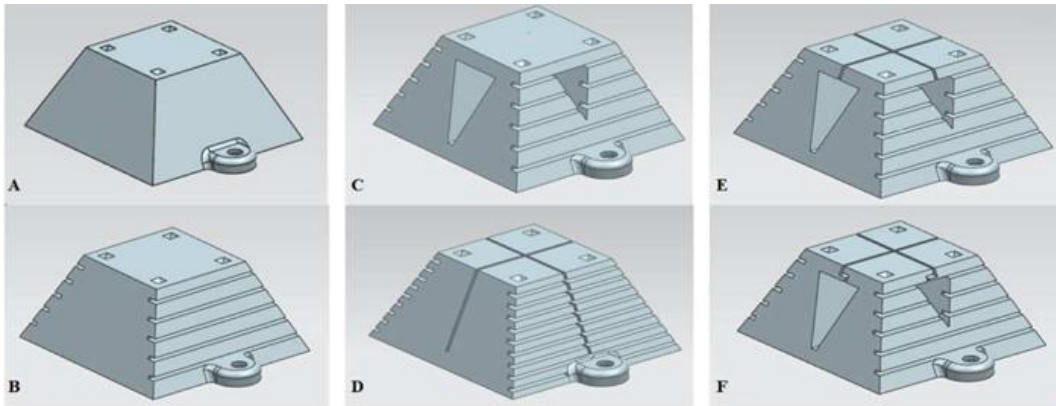

Image by "Simulated Design Strategies for SPECT Collimators to Reduce the Eddy Currents Induced by MRI Gradient Fields"[2]

D. RESULTS

Current Density on the Surface of the Collimator:

A comparison of the current density on the collimator surfaces across various modified designs shows a general decrease relative to the original design.

Temporal Variation of the Induced Field for the Original and the Optimized Ring of Collimators:

This analysis examined the induced magnetic induction due to eddy currents as a percentage of the applied gradient field for both longitudinal and transverse gradient coils (x- and y-gradient coils) for both the original and the optimized collimator rings, averaged within a field of view of 3 cm. The original collimator exhibited a maximum induced magnetic field of 4.21% and 1.06% of the applied gradient for longitudinal and transverse gradient coils, respectively, whereas the optimized ring displayed reduced values of 1.91% and 0.46% for the longitudinal and transverse gradient coils, respectively. Transverse coils consequently produced fewer eddy currents than their longitudinal counterparts, with maximum induced magnetic fields reduced to under 2% of the applied gradient field across both types.

IV. MINIMIZING MRI SUSCEPTIBILITYARTIFACTS IN IMPLANTS

METHODS

Specimen Manufacture: Specimens were crafted using a RenAM500M selective laser melting system (Renishaw, UK) located at the Centre for Custom Medical Devices. Samples comprised spherical Ti-6Al-4V (Grade 23 (RM1) from Renishaw) powder within a size range of 15 to 53 μm. Layers were processed with a thickness of 30 μm employing either a contour-only laser scanning strategy for diamond and octahedral lattice designs or a hatch-and-contour approach for honeycomb samples. The laser power and effective scanning speed for contour scanning were set to 100 W and 1125 mm/s, while 200 W and 1100 mm/s were allocated for hatched regimes.

MRI Measurements: Custom 3D printed polymer lattices (Stratasys, Object) were assembled as supports for the titanium samples and to establish geometric reference in the collected data. The metal lattices were placed upright in the polymer framework, positioned approximately 6 mm deep. To facilitate filling and allow for sample swaps, pre-boiled tap water was selected as the phantom medium to provide the MRI signal. The water was cooled to room temperature to expel gas and minimize air bubble formation within the lattice. Two polymer lattice assemblies were affixed to the base of each vessel, which were filled with water until the metal lattice was fully submerged several centimeters below the water surface. The vessel was placed on a vibrating platform for several minutes until no further air bubbles emerged from the metal lattice.

Statistical Methods: In instances where regression analysis occurred, the curve fitting and R^2 values are indicated in the figure captions. Given that each image sequence only produced a single MRI dataset, error bars were estimated based on variability associated with image resolution. For length measurements, error bars showed ±0.5 pixels, considering this linear interpolation. Consistent threshold values were utilized across specimens for volume measurements, and error bars represented a range of ±1 voxel over the entire surface area to accommodate noise.

RESULTS

Coronal images of diamond lattice structures obtained from the gradient echo sequence are displayed, showcasing (a) magnitude and (b) phase data, along with (c) a spin echo image, and a (d) longitudinal gradient echo image illustrating a vertical section of the specimen. Dark areas in the gradient echo magnitude images at the specimen edges indicate complete signal loss due to the susceptibility artifact, increasing in extent as relative lattice density rises from 17% to 72%. Comparative images obtained through the spin echo sequence (Fig. 4(c)) do not exhibit the same regions of total signal loss as seen in gradient echo sequences; however, both methods reveal distortion from field inconsistencies. Figures (a) and (c) underscore the disparities between these imaging techniques.
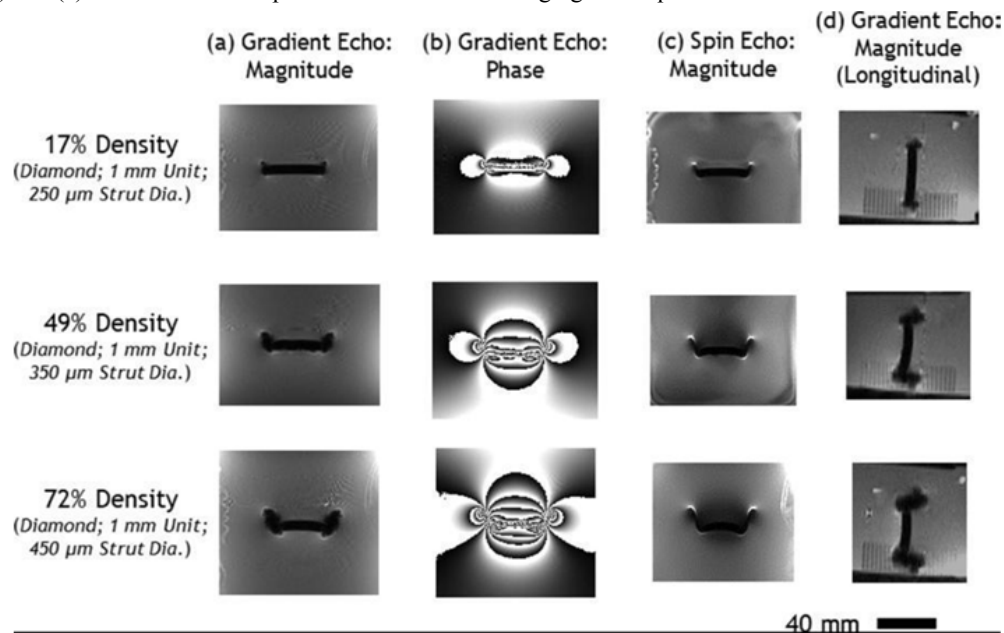

Image by "Reducing MRI susceptibility artefacts in implants using additively manufactured porous Ti-6Al-4V structures"[3]

Phase images reveal the extent of disruption in the measured signal's phase. Banding in these images results from the 'phase-wrapping' effect, where the phase, representing the orientation of a vector, cycles from -π to π. The pixel values fluctuate from minimum (black) to maximum (white) as the received signal crosses these limits. As with magnitude data, these images (Fig. (b)) indicate a larger affected region correlating with increasing sample density from 17% to

49% and 72%. The longitudinal gradient echo images (Fig. (d)) similarly portray 'edge-plumes' of artifacts above and below the specimen, akin to those observed in the coronal plane.

Additionally, images from the gradient echo sequence for metal lattice samples showcasing relative densities (29.4% - 30.8%) across three different unit cell designs (octahedral, diamond, and honeycomb) depict typical characteristics of the dataset without significant variations in artifact nature between the two designs (octahedral or diamond). In contrast, honeycomb samples manifest 'protrusions' of artifact volume visible in gradient echo magnitude images (evident in the detail of the honeycomb sample). These features relate to the honeycomb channels, appearing more prominent in larger cell sizes (6 mm and 4 mm). Thus, honeycomb artifacts seem to be more critical than their lattice counterparts for similar sample densities.

The volume of the signal loss region in gradient echo magnitude data was charted against sample relative density (Fig. (a)). A linear trendline fitting yielded an $R^2 = 0.97$; however, honeycomb samples deviated from this trend, especially at densities below 60% (noted as green squares in Fig. (a)). A trendline recalculated excluding honeycomb specimens displayed improved correlation with $R^2 = 0.99$. The honeycomb specimens' artifact volume is separately plotted in Fig. (d) correlated to each unit cell size, indicating escalating artifact severity with increasing cell size. The 4 mm cells displayed an average artifact volume increase of 3700 mm³ while 6 mm cells showed a rise of 4300 mm³ compared to the baseline lattice trend. The typical MRI gradient echo magnitude images for all specimens analyzed appear in Supplemental Figure S1. An assessment of artifact displacement from expected positioning revealed a similar positive correlation with density (Fig. (b)). Nonetheless, a second-order polynomial relationship was determined to optimally fit this data ($R^2 = 0.92$), with no apparent outliers identified. Fig. (c) illustrates the distance between the outermost phase wrap as an approximation of artifact extent. A transition in gradient was observed alongside a visible alteration in the shape of the outer phase wrap boundary transitioning from a flattened to a rounded shape (as shown in the inset images of Fig. (c)). This transition occurred roughly at 45% relative density and corresponds to a distance about equal to the specimen's width (42 mm).
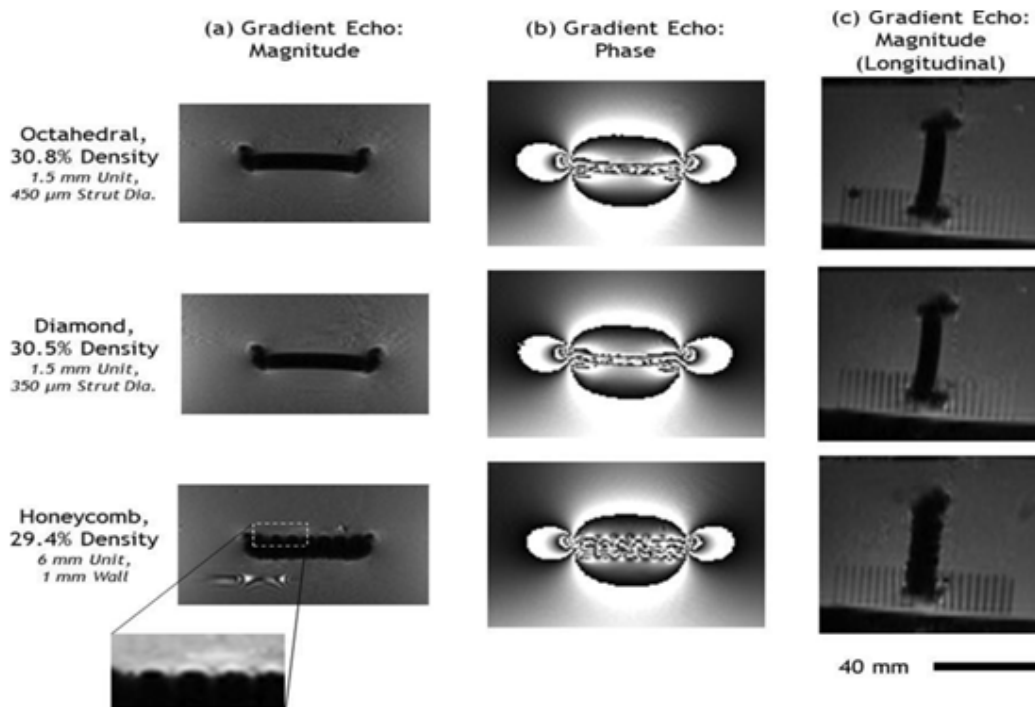

Image by "Reducing MRI susceptibility artefacts in implants using additively manufactured porous Ti-6Al-4V structures"[3]

V .THE ACCURACY OF ULTRASORT ECHO TIME MRI SEQUENCES FOR MEDICALADDITIVE MANUFACTURING

METHODS

A MRI scanner were used to scan the three dry mandibles (Step1), and an optical 3D scanner (Artec Spider; Artec group, Moscow, Russia) was used to capture an optical scan of all three mandibles with a point accuracy of 0.05 mm. The "goldstandard" STL models were the optical scans of the three mandibles. After that, the MRI scans were aligned with the gold-standard STL models and converted to STL files (Step 2). The geometric differences between the gold-standard models and the STL models obtained from MRI were then computed. In order to map additional geometric deviations introduced during the AM process, the MRI and gold-standard STL model of one mandible were also additively built (Step 3) and scanned again using an optical scanner (Step4).
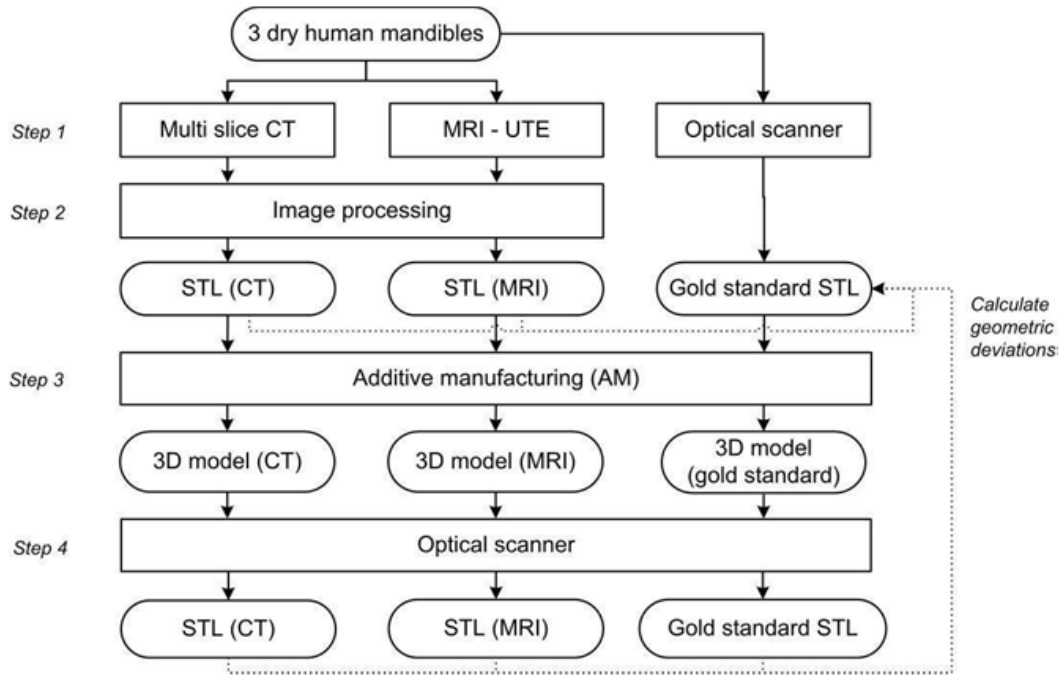
(Figure 1) Outline of the study. STL, Standard Tessellation Language; UTE, ultrashort echo time.

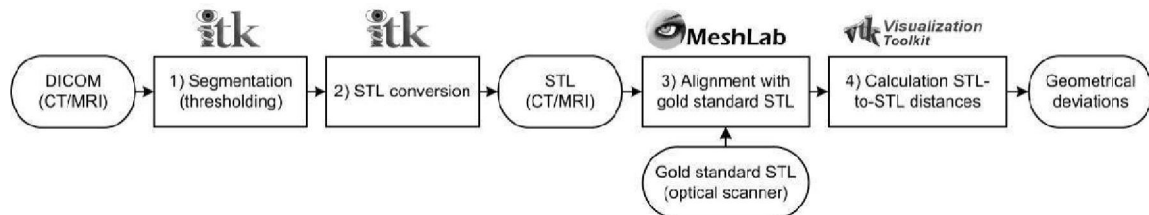Image by "The accuracy of ultrashort echo time MRI sequences for medical additive manufacturing"[4]

MRI:

Conventional spin or gradient echo sequences are too slow to pick up any bone signal because the mandibular cortical bone has a very short $T2*$ of about 1.5 ms. UTE imaging produces an MR signal from the surrounding cortical bone by directly sampling the free induction decay signal with an echo duration of less than one millisecond. A Philips Achieva® 3-T MRI scanner (Philips Healthcare, Best, Netherlands) equipped with an eight-channel head radio-frequency coil and a UTE single-echo sequence was used to scan all three mandibles. The scan parameters that were employed were flip angle = 15°, echo time1 = 0.14 ms, and repetition time = 4.8 ms. After stimulation with a non-selective harsh radio-frequency pulse, the receive coil was tuned. Free induction decay sampling was then initiated while the gradients ramped up. The time between excitation and readout as a result of this process was 0.14 ms. The 3D k-space was regridded to a Cartesian coordinate system of isotropic 0.5 x 0.5 x 0.5-mm voxels after being radially sampled.
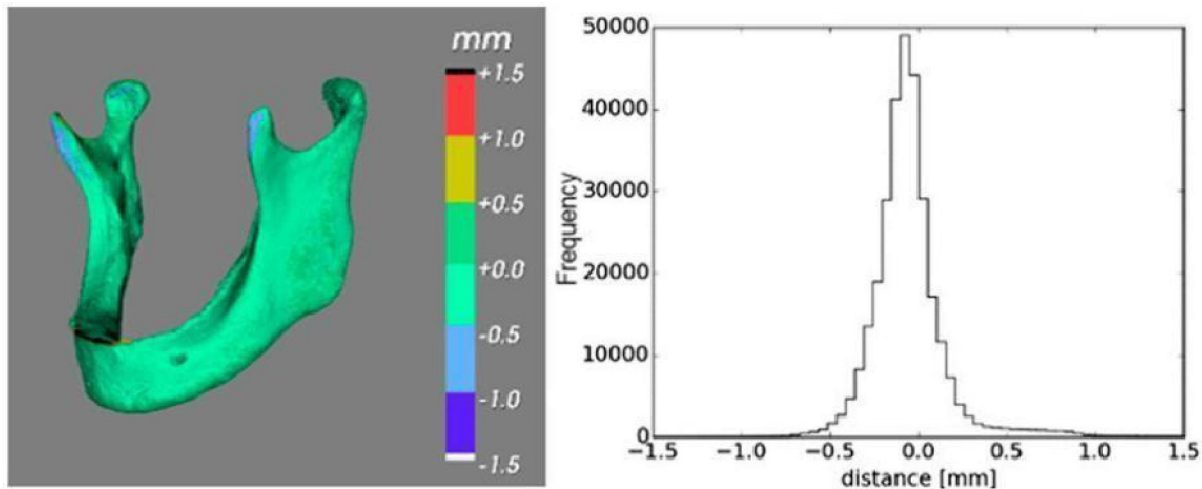
THE USE OF ADDITIVE MANUFACTURING:

GOM Inspect® software (GOM mbH, Braunschweig, Germany) was used to import the MRI-derived STL models of Mandible 1 and smooth them with a surface tolerance of 1.0 mm in order to adjust for stair-step artifacts. A Z printer 250 inkjet powder printer (3D Systems Inc., Rock Hill, SC) was used to print the gold standard STL model of Mandible 1 acquired using the optical scanner as well as the smoothed MRI-derived STL model. In accordance with Steps 3 and 4, the final additively produced models were scanned once again using an optical scanner, aligned with the gold-standard STL model, and then submitted to STL deviation analysis in Figure 2.

(Figure 2) *Overview of image processing steps and software packages involved in the STL analysis.*
Image by "The accuracy of ultrashort echo time MRI sequences for medical additive manufacturing"[4]

RESULTS

With the exception of Mandible 1 (1.69 mm), all geometric discrepancies between the MRI-derived STL models and the optical scan goldstandard STL models were typically less than 2.0 mm, with 95th percentiles less than 1.5 mm. All MRI-derived STL models displayed a greater spread of deviations in the mandibular condyles and a smaller spread in the symphyseal area. The additively produced 3D models of Mandible 1 showed a few more minor geometric aberrations (Figure A). Geometric variations of up to 0.5 mm were shown by the additively produced goldstandard 3D model, particularly in thin components like the alveolar ridge and coronoid process.Deviations were noted in the coronoid process, mandibular condyles, and alveolar ridge of the 3D model created using MRI data (Figure B).

(Figure A) AM 3D Model Gold-Standard
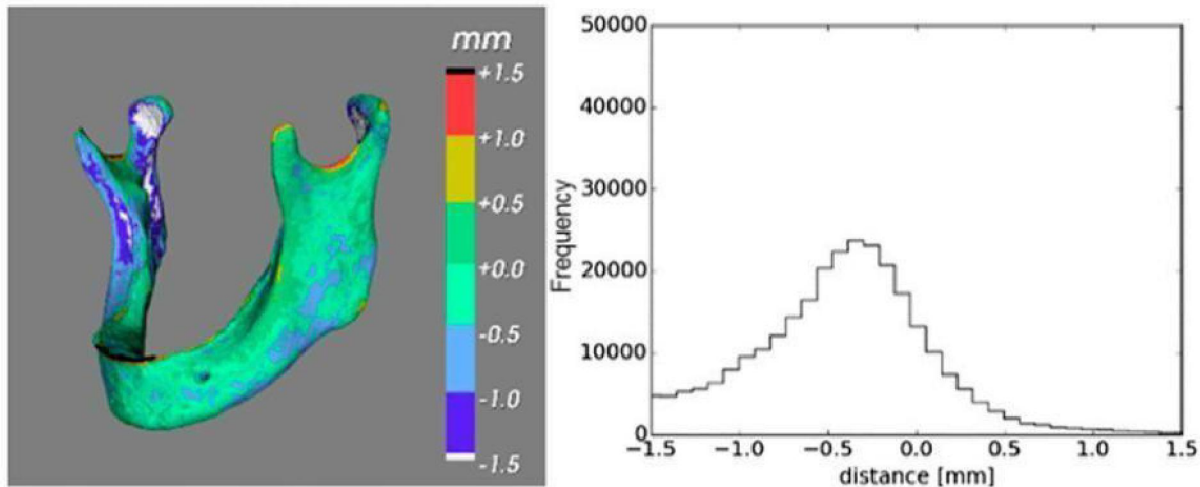
(Figure B) AM Model-MRI

Image by "The accuracy of ultrashort echo time MRI sequences for medical additive manufacturing"[4]

VI .CONCLUSION

This study has shown that additive manufacturing techniques can be effectively utilized to create macroscopic coils without any technical constraints. We can fabricate coils of several centimeters in size using existing setups (like Fab@home) or larger coils with slight adjustments. Importantly, the achieved conductivities are nearly equal to bulk conductivity. As seen in other applications of computer-controlled numerical machining, we believe that our approach aligns well with the simulations typically used to optimize gradient coil designs. We envision no other viable method for implementing fractal cooling schemes that could greatly enhance duty cycles at the high power levels needed by MRI gradient systems. This project encourages MRI designers to engage with the dynamic additive manufacturing community.

We addressed and minimized the induced magnetic field resulting from eddy currents in a complete ring of collimators designed for an MRI system. A numerical model was created to analyze the x-, y-, and z-gradient coils with various collimator designs, focusing on the eddy currents produced in the tungsten collimators due to gradient fields in the MRI system. Simulations were performed with a 3D electromagnetic simulator equipped with a time analysis tool. Alterations were made to the collimator's surface and design, reducing the maximum induced magnetic field by 51%, enhancing MR compatibility. The numerical model and simulation tool were validated accordingly. We conclude that printed tungsten collimators are suitable for use in combined MRI systems.

For octahedral and diamond lattice structures, the artifact volume correlates linearly with relative density ($R^2 = 0.99$). A 50% reduction in mass resulted in a 50% decrease in artifact volume. Conversely, honeycomb structures displayed a slightly higher artifact volume than anticipated for their relative density when evaluating larger unit cell sizes (6 mm yielding a 4300 mm³ increase; 4 mm a 3700 mm³ increase). Notably, artifact displacement strongly correlated with sample density ($R^2 = 0.92$) due to B0 field distortion caused by the metal lattice, which led to skewed slice selection. Phase imaging illustrated the extent of disruption caused by metal samples, with severity measurements confirming a positive correlation with relative density similar to the magnitude data. The overall pattern of phase disruption seemed influenced by both density and geometry, suggesting a fascinating area for future research. Importantly, relative density emerged as a crucial factor driving artifact behavior around the lattice specimens, rather than unit cell type, size, or strut diameter.

This research demonstrates that the use of UTE MRI for imaging bone is a viable alternative to CT for generating STL models of mandibles with varied morphologies, making it suitable for surgical planning and additive manufacturing. Both CT and MRI methods typically introduced geometric deviations of less than 1.0 mm and less than 1.5 mm,

respectively, while the additive manufacturing process added minor deviations of less than 0.5 mm. Additional in vivo studies are needed to evaluate the viability of the UTE MRI sequence in clinical scenarios.

REFERENCES

[1]. Goodbye Wires and Formers: 3-D Additive Manufacturing and Fractal Cooling Applied to Construction of MRI Gradient Coils, Mario G. Urdaneta, Roland Probst, Pavel Y. Stepanov, Irving N. Weinberg, Members, IEEE, and Stanley T. Fricke, 2011 IEEE Nuclear Science Symposium Conference Record

[2]. Simulated Design Strategies for SPECT Collimators to Reduce the Eddy Currents Induced by MRI Gradient Fields, Amine M. Samoudi, Karen Van Audenhaege, GünterVermeeren, Gregory Verhoyen, Luc Martens, Roel Van Holen, and Wout Joseph IEEE TRANSACTIONS ON NUCLEAR SCIENCE, VOL. 62, NO. 5, OCTOBER 2015

[3]. Reducing MRI susceptibility artefacts in implants using additively manufactured porous Ti-6Al-4V structures, Luke N. Carter a , Owen Addison b , , Nashwan Naji c , Peter Seres c , Alan H. Wilman c , Duncan E.T. Shepherd d , Liam Grover a , Sophie Cox a

[4]. The accuracy of ultrashort echo time MRI sequences for medical additive manufacturing 1Maureen van Eijnatten, 2Erik-Jan Rijkhorst, 2Mark Hofman, 1Tymour Forouzanfar and 1Jan Wolff 1Department of Oral and Maxillofacial Surgery/Oral Pathology and 3D InnovationLab, VU University Medical Center, Amsterdam, Netherlands; 2Department of Physics and Medical Technology, VU University Medical Center, Amsterdam, Netherlands

[5]. Progress and Prospects of Additive Manufacturing in Lightweight Design, Wentao Xu* ,School of Mechanical Engineering, Changshu Institute of Technology, Changshu, 324100, China * Corresponding Author Email:C073120126@cslg.edu.cn

[6]. Rapid additive manufacturing of MR compatible multipinhole collimators with selective laser melting of tungsten powder, Karel Deprez, Stefaan Vandenberghe, Karen Van Audenhaege, Jonas Van Vaerenbergh, and Roel Van Holen

[7]. Gradient coil design using Bi-2223 high temperature superconducting tape for magnetic resonance imaging, Jing Yuan, G.X. Shen MRI Lab, Department of Electrical and Electronic Engineering, The University of Hong Kong, Pokfulam Road, Hong Kong

[8]. Winding Resistance and Power Loss of Inductors With Litz and SolidRound Wires Rafal P. Wojda and Marian K. Kazimierczuk Fellow, IEEE

[9]. A novel, cylindrical, transverse gradient coil design for magnetic resonance imaging of large samples, S Di Luzioy, G Placidiyz, S Di Giuseppey, M Alecciy and A Sotgiuy INFM, c/o Department of Biomedical Sciences, University of L'Aquila, Via Vetoio 10, 67100 L'Aquila, Italy z Department of Electrical Engineering, University of L'Aquila, Roio Poggio, 67100L'Aquila, Italy

[10]. Thermal Modeling of Inductor and Transformer Windings Including Litz Wire Phyo Aung Kyaw, Student Member, IEEE, Myl`eneDelhommais, Student Member, IEEE, Jizheng Qiu, Charles R. Sullivan, Fellow, IEEE, Jean-Luc Schanen, Senior Member, IEEE and C´ecile Rigaud

[11]. Design and fabrication of a three-axis multilayer gradient coil for magnetic resonance microscopy of mice Blaine Chronika,c, Andrew Alejski c, BrianK.Rutta,b,c,* a Department of Physics and Astronomy, Uni6ersity of Western Ontario, Ont., Canada b Department of Diagnostic Radiology and Nuclear Medicine, Uni6ersity of Western Ontario, Ont.,Canada c Imaging Research Laboratories, The John P. Robarts Research Institute, P.O. Box 5015, 100 Perth Dri6e, London, Ont., Canada N6A 5K8

[12]. Additive Manufacturing of Tungsten Carbide Hardmetal Parts by Selective Laser Melting (SLM), Selective Laser Sintering (SLS) and Binder Jet 3D Printing (BJ3DP) Techniques, Padmakumar M.1 Springer Science+Business Media, LLC, part of Springer Nature 2020

[13]. Accurate Calculation and Sensitivity Analysis of Leakage Inductance of High-Frequency Transformer with Litz Wire Winding, Ke Zhang, Wu Chen, Senio Member, IEEE, Xiaopeng Cao, Pengpeng Pan, Syed Waqar Azeem, Guangyao Qiao and Fujin Deng

[14]. Theory of Gradient Coil Design Methods for Magnetic Resonance Imaging S.S. HIDALGO-TOBON Departamento de Ingenieria Electrica, Universidad Auto´nomaMetropolitanaIztapalapa, Av. San Rafael Atlixco 186, Me´xico D.F. 09340, Me´xico

[15]. Winding resistance of litz-wire and multi-strand inductors Department of Electrical Engineering, Wright State University, 3640 Colonel GlennHighway, Dayton 45435 OH, USA E-mail:rafal.wojda@fulbrightmail.org

[16]. Design and Additive Manufacturing of MRI Gradient Coils,J.P.Rigla, A. Sarwar, A. Nacev, M.G. Urdaneta, E. Anashkin, P. Stepanov, I.N. Weinberg, J.M. Benlloch, A. McMillan, R. Hilaman, and S.T. Fricke

[17]. C. L. G. Ham and J. Konijn, "MRI Apparatus," 6822452, November 23, 2004.

[18]. K. Nayak and B. Hu, "The Future of Real-Time Cardiac Magnetic Resonance Imaging," Current Cardiology Reports, vol. 7, pp. 45-51, 2005.

[19]. "Working Group Report on Magnetic Resonance Imaging - Hardware," ed: Industry Canada (Medical Imaging Technology Roadmap), 2008.

[20]. C. R. Sullivan, "Cost-Constrained Selection of Strand Wire and Number in a Litz-Wire Transformer Winding," IEEE Transactions on Power Electronics, vol. 16, pp. 281-288, 2001.

[21]. F. D. Doty, MRI Gradient Coil Optimization: Wiley-VCH Verlag GmbH, 2007.

[22]. B. Chronik, A. Alejski, and B. Rutt, "Design and fabriacation of a three axis multilayer gradient coil for magnetic resonance microscopy of mice," Magnetic Resonance Materials in Physics, Biology and Medicine, vol. 10, pp. 131-146,2000.

[23]. I N. Weinberg, P. Stepanov, S. C. Glidden, H. D. Sanders, D. Wamow,A.B.McMillan, R. P. Gullapalli, K.-M. Lo, A. Fisher, J. P. Reilly, M. S. Niziol, and S. T. Fricke, "Threshold for Peripheral Nerve Stimulation with Ultra-Fast Gradients," Proceedings of the International Society for Magnetic Resonance in Medicine, 2011.

[24]. V. Sanchez-Romaguera, M.-8. Madec, and S. G. Yeates, "Inkjet printingof 3D metal-insulator-metal crossovers," Reactive and Functional Polymers, vol. 68, pp. 1052-1058,2008.

[25]. E. Malone and H. Lipson, "Fab@Home: the personal desktop fabricatorkit," Rapid Prototyping, vol. 13, pp. 245-255, 2007.

[26]. H. Zaidi, N. Ojha, and M. Morich et al., "Design and performanceevaluation of a whole-body ingenuity TF PET-MRI system," Phys. Med. Biol., vol. 21, pp. 3091–3106, 2011.

[27]. G. Delso, S. Furst, and B. Jakoby et al., "Performance measurements ofthe siemens mMR integrated whole-body PET/MR scanner," J. Nucl. Med., vol. 52, pp. 1914–1922, 2011.

[28]. C. Goetz, E. Breton, P. Choquet, V. Israel-Jost, and A. Constantinesco,"SPECT low-field MRI system for small-animal imaging,"J.Nucl. Med., vol. 49, pp. 88–93, 2008.

[29]. M. Hamamura, S. Ha, W. Roeck, T. Muftuler, D. Wagenaar, D. Meier,B. Patt, and O. Nalcioglu, "Development of an MR-compatible SPECT system (MRSPECT) for simultaneous data acquisition," Phys. Med. Biol., no. 55, pp. 1563–1575, 2010, 2010.

[30]. L. Cai, X. Lai, Z. Shen, C. T. Chen, and L. J. Meng, "MRC-SPECT: A sub-500 mm resolution MR-compatible SPECT system for simultaneous dual-modality study of small animals," Nucl. Instrum. Methods Phys. Res. A, vol. 734, pp. 147–151, 2014.

[31]. P. Busca et al., "Simulation of the expected performance of INSERT: A new multi-modality SPECT/MRI system for preclinical and clinical imaging," Nucl. Instrum. Methods Phys. Res. A, vol. 734, pp. 141–146, 2014.

[32]. Mediso Medical Imaging Systems [Online]. Available: http://www. mediso.com, Apr. 2015

[33]. A Samoudi, K. Van Audenhaege, G. Vermeeren, M. Poole, L. Martens,R.Van Holen, and W. Joseph, "Influence of collimator insertion on eddy currents for different resistivities of tungsten," in Proc. Int. Soc. Mag. Reson. Med., 2014, vol. 22, p. 2824.

[34]. Samoudi, K. Van Audenhaege, G. Vermeeren, M. Poole, L.Martens,R.Van Holen, and W. Joseph, "Temporal analysis of z-gradient coil eddy currents in tungsten collimator with different resistivities for SPECT/MRI," in Proc. 3rd PSMR Conf. PET/MR and SPECT/MR, EJNMMI Physics, 2014, vol. 1, no. 1 (suppl. 1):A22.

[35]. M. A. Morich, D. A. Lampman, W. R. Dannels, Handler, and F. T. D. Goldie, "Exact temporal eddy current compensation in magnetic resonance imaging systems," IEEE Med. Imag., vol. 7, pp. 247– 254 1988.

[36]. S. Crozier, C. Eccles, F. Beckey, J. Fields, and D. Doddrell,"Correction of eddy current-induced B0 shifts by receiver reference phase modulation," J. Magn. Reson., vol. 97, pp. 661–665, 1992.

[37]. A Samoudi, K. Van Audenhaege, G. Vermeeren, M. Poole, E. Tanghe,L. Martens, R. Van Holen, and W. Joseph, "Analysis of eddy currents induced by transverse and longitudinal gradient coils in different tungsten collimators geometries for SPECT/MRI integration," Magn. Reson. Med., 2014, doi: 10.1002/mrm.25534.

[38]. K. Deprez, S. Vandenberghe, K. V. Audenhaege, J. V. Vaerenbergh,andR.V.Holen, "Rapid additive manufacturing of MR compatible multipinhole collimators with selective laser melting of tungsten powder," Med. Phys., vol. 40, 2013.

[39]. M. Poole and R. Bowtell, "Novel gradient coils designed using aboundary element method," Concepts Magn. Reson., vol. B31, pp. 162– 175, 2007.

[40]. K. Deprez, R. Van Holen, and S. Vandenberghe, "The lofthole: Anovel shaped pinhole geometry for optimal detector usage without multiplexing and without additional shielding," in Proc. IEEE Nuclear Science Symp. and Medical Imaging Conf. Rec., 2011, pp. 3317–3322.

[41]. R. Van Holen, B. Vandeghinste, K. Deprez, and S. Vandenberghe, "Design and performance of a compact and stationary microSPECT system," Med. Phys., vol. 40, no. 11, p. 112501, 2013.

[42]. M. A. Bernstein, K. F. King, and X. Zhou, Handbook of MRI Pulse Sequences. Boston, MA, USA: Academic, 2004.

[43]. M. Negrazus, D. George, V. Vrankovic, and M. Werner, "Eddy current reduction in fast ramped bending magnets," IEEE Trans. Appl.Supercond., vol. 16, no. 2, pp. 228–230, 2006.

[44]. Ramasamy M, Giri, Raja R, Subramonian, Karthik, Narendrakumar R. Implant surgical guides: from the past to the present.J Pharm Bioallied Sci 2013; 5: S98–102. doi: http://dx.doi.org/10.4103/0975-7406.113306

[45]. Voss JO, Varjas V, Raguse JD, Thieme N, Richards RG, Kamer L. Computed tomography-based virtual fracture reduction techniques in bimandibular fractures. J CraniomaxillofacSurg 2016; 44: 177–85. doi: http://dx.doi.org/10.1016/j.jcms.2015.11.010

[46]. Yu H, Wang X, Zhang S, Zhang L, Xin P, Shen SG. Navigationguideden bloc resection and defect reconstruction of craniomaxillary bony tumours. Int J Oral MaxillofacSurg 2013; 42:1409–13. doi: http://dx.doi.org/10.1016/j.ijom.2013.05.011

[47]. Schepers RH, Kraeima J, Vissink A, Lahoda LU, Roodenburg JL, Reintsema H, et al. Accuracy of secondary maxillofacial reconstruction with prefabricated fibula grafts using 3D planning and guided reconstruction. J CraniomaxillofacSurg Jan 2016. Epub ahead ofprint. doi: http://dx.doi.org/10.1016/j.jcms.2015.12.008

[48]. Li Y, Jiang Y, Ye B, Hu J, Chen Q, Zhu S. Treatment of dentofacial deformities secondary to osteochondroma of the mandibular condyle using virtual surgical planning and 3-dimensional printed surgical templates. J Oral MaxillofacSurg 2016; 74: 349–68. doi: http://dx.doi.org/10.1016/j.joms.2015.06.169

[49]. Dawood A, Marti BM, Sauret-Jackson V, Darwood A. 3D printing in dentistry. Br Dent J 2015; 219: 521–9. doi: http://dx. doi.org/10.1038/sj.bdj.2015.914

[50]. Mazzoni S, Bianchi A, Schiariti G, Badiali G, Marchetti C. Computeraided design and computer-aided manufacturing cutting guides and customized titanium plates are useful in upper maxilla waferless repositioning. J Oral MaxillofacSurg 2015; 73: 701–7. doi:http://dx.doi.org/10.1016/j.joms.2014.10.028

[51]. Kontio R. Update on mandibular reconstruction: computer-aided design, imaging, stem cells and future applications. Curr OpinOtolaryngol Head Neck Surg 2014; 22: 307–15. doi: http://dx.doi.org/10.1097/MOO.0000000000000065

[52]. Aguiar MF, Marques AP, Carvalho AC, Cavalcanti MG. Accuracy of magnetic resonance imaging compared with computed tomography for implant planning. Clin OralImplants Res 2008; 19: 362–5. doi:http://dx.doi.org/10.1111/ j.1600-0501.2007.01490.x

[53]. Keereman V, Fierens Y, Broux T, De Deene Y, LonneuxM,VandenbergheS. MRI-based attenuation correction for PET/ MRI using ultrashort echo time sequences. J Nucl Med 2010; 51:812–18. doi: http://dx.doi.org/10.2967/jnumed.109.065425

[54]. Aitken AP, Giese D, Tsoumpas C, Schleyer P, Kozerke S, PrietoC, et al. Improved UTE-based attenuation correction for cranialPET-MR using dynamic magnetic field monitoring. Med Phys 2014; 41: 012302. doi: http://dx.doi.org/10.1118/1.4837315